Title
Seismic and aseismic deformations and impact on reservoir permeability: The case of EGS stimulation at The Geysers, California, USA

Permalink
https://escholarship.org/uc/item/8pc2m7wr

Journal
Journal of Geophysical Research: Solid Earth, 120(11)

ISSN
2169-9313

Authors
Jeanne, Pierre
Rutqvist, Jonny
Rinaldi, Antonio Pio
et al.

Publication Date
2015-11-01

DOI
10.1002/2015jb012142

Peer reviewed

RESEARCH ARTICLE

Key Points:
- Presence of injected water leads to the development of an aseismic domain
- Permeability gain mostly occurs inside the aseismic domain
- Thermal processes may be responsible for the appearance of aseismic deformations

Correspondence to:
P. Jeanne,
pjeanne@lbl.gov

Seismic and aseismic deformations and impact on reservoir permeability: The case of EGS stimulation at The Geysers, California, USA

Pierre Jeanne[1], Jonny Rutqvist[1], Antonio Pio Rinaldi[2], Patrick F. Dobson[1], Mark Walters[3], Craig Hartline[3], and Julio Garcia[3]

[1]Earth Science Division, Lawrence Berkeley National Laboratory, Berkeley, California, USA, [2]Swiss Seismological Service, Swiss Federal Institute of Technology, ETHZ, Zürich, Switzerland, [3]Calpine Corporation, Middletown, California, USA

Abstract In this paper, we use the Seismicity-Based Reservoir Characterization approach to study the spatiotemporal dynamics of an injection-induced microseismic cloud, monitored during the stimulation of an enhanced geothermal system, and associated with the Northwest Geysers Enhanced Geothermal System (EGS) Demonstration project (California). We identified the development of a seismically quiet domain around the injection well surrounded by a seismically active domain. Then we compare these observations with the results of 3-D Thermo-Hydro-Mechanical simulations of the EGS, which accounts for changes in permeability as a function of the effective normal stress and the plastic strain. The results of our modeling show that (1) the aseismic domain is caused by both the presence of the injected cold water and by thermal processes. These thermal processes cause a cooling-stress reduction, which prevent shear reactivation and favors fracture opening by reducing effective normal stress and locally increasing the permeability. This process is accompanied by aseismic plastic shear strain. (2) In the seismic domain, microseismicity is caused by the reactivation of the preexisting fractures, resulting from an increase in injection-induced pore pressure. Our modeling indicates that in this domain, permeability evolves according to the effective normal stress acting on the shear zones, whereas shearing of preexisting fractures may have a low impact on permeability. We attribute this lack of permeability gain to the fact that the initial permeabilities of these preexisting fractures are already high (up to 2 orders of magnitude higher than the host rock) and may already be fully dilated by past tectonic straining.

1. Introduction

Injection-induced seismicity has become an important topic from both scientific and economic perspectives. Injecting fluid into a rock formation reduces the effective stress and can lead to brittle failure [*Terzaghi*, 1923]. The creation and/or reactivation of fractures can enhance access to the reservoir fluids (oil, gas, or geothermal energy), while microseismicity may be induced due to the release of preexisting tectonic stresses. Therefore, microseismic monitoring can be a useful source of information about ongoing reservoir stimulation. Analysis of microseismic activity can yield valuable information regarding the extent of a stimulation zone [*Rutqvist et al.*, 2015], in situ stress field [*Boyle and Zoback*, 2013], fracture orientation [*Verdon et al.*, 2011], fault zone location [*Jeanne et al.*, 2014a], and on reservoir hydromechanical properties [*Jeanne et al.*, 2014b]. In geothermal activities, and especially during Enhanced Geothermal System (EGS) development, induced seismicity can be used to image fluid pathways generated by hydraulic stimulation treatments [*Jeanne et al.*, 2014a]. The occurrence of microseismicity at a point remote from the injection interval may indicate that the point has a hydraulic connection to the borehole interval. However, it does not necessarily mean that significant hydraulic flow occurs along the connection [*Cornet and Scotti*, 1993]. Moreover, when a preexisting fracture is reactivated, it is very hard to quantify changes in permeability from the seismic signals. Therefore, it is generally very difficult to identify where the injected water flows [*Baisch et al.*, 2002] and where the most significant changes in reservoir hydraulic and mechanical properties occur. Nevertheless, such changes in properties may profoundly affect the evolution of the stimulated region [*Rinaldi et al.*, 2014].

Also, during reservoir stimulation, aseismic deformations (plastic or elastic) can occur, modifying the reservoir permeability. Laboratory and field tests have shown that rock permeability is related to fracture aperture and to the effective stress normal to the fracture [*Liu et al.*, 2004; *Rutqvist*, 2015]. During injection, pressurization of

the rock mass can lead to elastic deformation of preexisting fractures, temporarily modifying their aperture and thus their permeability [*Guglielmi et al.*, 2008]. Moreover, nonlinear deformation and shear dilation associated with the reactivation of preexisting fractures can significantly change rock-mass permeability [*Rutqvist*, 2015; *Min et al.*, 2004]. In this paper, we present data collected during the stimulation associated with the Northwest Geysers EGS Demonstration Project, California [*Garcia et al.*, 2012; *Rutqvist et al.*, 2015]. This project aims to develop an EGS by directly and systematically injecting cool water at relatively low pressure beneath a vapor-dominated geothermal reservoir, where temperatures up to 400°C have been encountered. We focus our study on the relation between the formation of an injection-induced liquid saturated zone, the distribution of seismic and aseismic deformations, and changes in permeability. First, we present the study area, the injection strategy, and the monitoring system deployed to follow the EGS development. Then, we study the distribution of the microseismic events by using the Seismicity-Based Reservoir Characterization (SBRC) approach [*Shapiro et al.*, 1997, 2002] and compare these results with the results of a three-dimensional Thermo-Hydro-Mechanical (THM) numerical model simulation, accounting for changes in permeability related to both elastic changes in effective normal stress and plastic shear and tensile strain.

2. The Northwest Geysers EGS Demonstration Project

2.1. Geological Setting

The Northwest Geysers EGS Demonstration Project is located in the northwest part of The Geysers geothermal field, where a relatively shallow high temperature reservoir (HTR) up to 400°C has been identified extending downward from 2.6 km below the ground surface. The HTR underlies a normal temperature reservoir (NTR) located between 1.6 and 2.6 km below the surface, where temperatures are ~240°C [*Garcia et al.*, 2012]. The rocks are composed of graywacke in the NTR and of contact metamorphosed biotite hornfelsic metagraywacke ("hornfels") in the HTR. These two geothermal reservoirs are bounded above by very low permeability formations ("graywacke caprock") and below by granitic intrusions ("felsite") encountered at a depth of ~4.0 km. The reservoir rock at The Geysers is highly fractured, and very small perturbations of the stress field could induce seismicity [*Lockner et al.*, 1982; *Oppenheimer*, 1986; *Rutqvist et al.*, 2015].

Jeanne et al. [2014a] found that the EGS area is affected by a shear zone network composed of eight northwest striking (N130) shear zones oriented along the regional structural strike in the North Coast Ranges [e.g., *Hulen and Norton*, 2000], along with three northeast-striking (N050) shear zones (Figure 1a). The steam entries present along the injection well (black dots along P32 in Figure 1a) correspond to the intersections with near-vertical shear zones trending N130 spaced about 150 to 200 m apart. A study of the daily spatial evolution of the seismic events helped to identify this shear zone network [*Jeanne et al.*, 2014a], and its existence was corroborated by the analyses of the vertical ground surface deformation monitored by satellite from May 2011 (6 months before injection began) to September 2012 [*Jeanne et al.*, 2014b]. This shear zone network belongs to the Riedel system formed within the regional strike-slip fault zone system of the North Coast Ranges [*Nielson et al.*, 1991].

2.2. Injection Strategy

In the Northwest Geysers area, two previously abandoned exploratory wells, Prati 32 (P32) and Prati State 31 (PS31), were reopened as an injection/production pair for the EGS Demonstration Project [*Garcia et al.*, 2012]. One of the reopened wells (P32) was deepened to penetrate a thick portion of the HTR and was dedicated as an injection well. Three other wells—PS31, Prati 38 (P38), and Prati 25 (P25) (this last one was reopened as a steam production well partway through the injection period)—were used to monitor fluid pressure variations inside the reservoir during the initial (stimulation) injection in P32 (Figure 1), which began on 6 October 2011.

Water was injected at a relatively low rate, and bottom-hole pressure was kept much lower than the estimated minimum principal compressive stress at the injection depth [*Rutqvist et al.*, 2015]. The aim was to avoid propagation of a single hydraulic fracture but to create a more pervasive stimulation zone by dilating a network of preexisting fractures though shear reactivation. According to the usual startup procedure for new injection wells at The Geysers, a high initial rate of 60–65 kg/s (1000–1100 gpm (gallons per minute)) was used to collapse the steam bubble in the well bore and nearby formation, so that the injected water was drawn into the well and surrounding rock. This high rate of injection, initiated on 6 October 2011, was continued for 24 h and then reduced to ~25 kg/s (400 gpm) for the next 55 days. During this period, two injectivity (step rate) tests were conducted (17 October 2011 and 12 November 2011), in which the
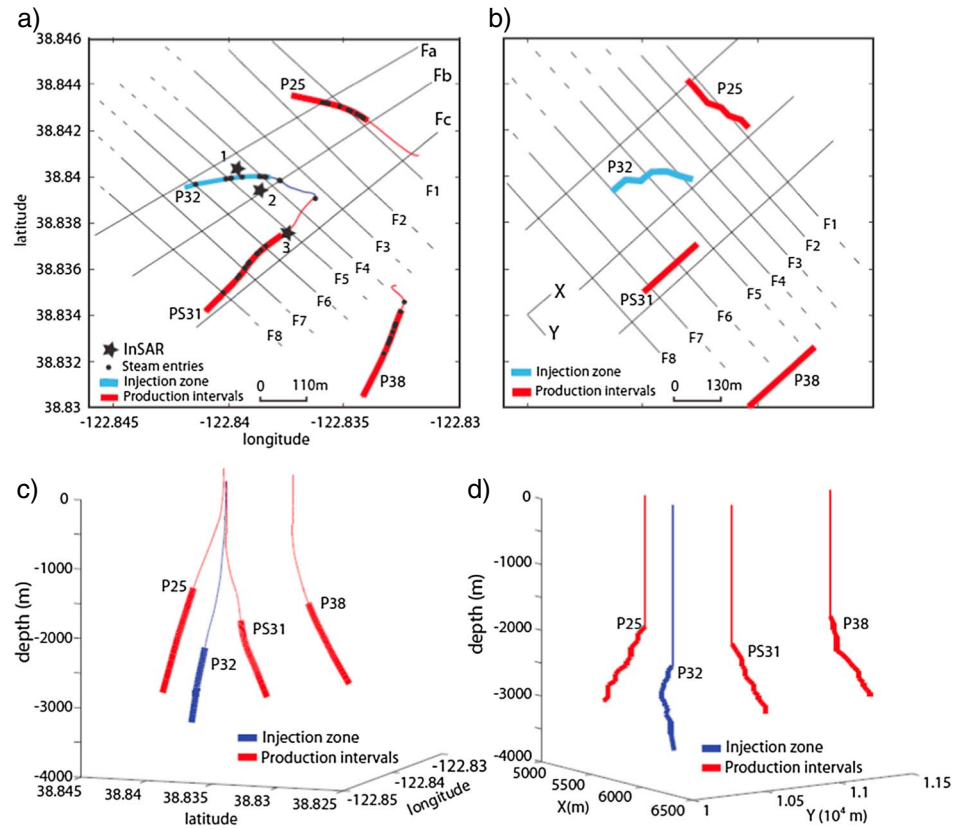
Figure 1. Comparison between the study area where the Northwest Geysers EGS Demonstration Project is performed and the geometric configuration of the 3-D model. (a) Structural map with the well locations P25, PS31, P32, and P38, including steam entries (black dots) and interferometric synthetic aperture radar monitoring data points (black stars) used in previous modeling [*Jeanne et al.*, 2014b]. (b) Plan view of the model geometry. Three-dimensional view of the wells (c) in the field and (d) in the model.

injection rate was increased in three steps and maintained for 1 h at a rate approximately equal to 38, 56, and 75 kg/s (600, 900, and 1200 gpm).

From these two tests, no apparent injectivity gain was observed [*Garcia et al.*, 2012], despite the fact that 112 microseismic events were recorded from the beginning of injection to 17 October 2011; and 291 additional microseismic events were recorded from 17 October 2011 to 15 November 2011. Therefore, in order to increase the stimulation effect around P32, and to investigate the effect of the injection rate on the microseismic response, the injection rate was increased from 25 kg/s to 63 kg/s (400 to 1000 gpm)
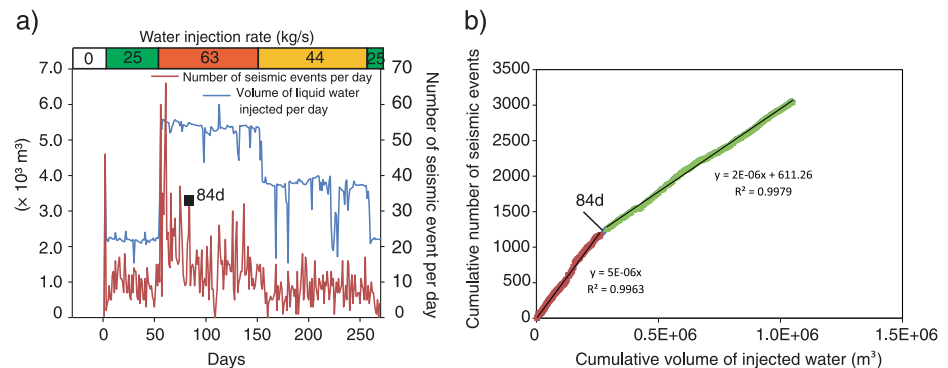

Figure 2. (a) Daily evolution of the number of microseismic events and the rate of liquid water injected. (b) Relation between the cumulative number of seismic events and the cumulative volume of injected water.
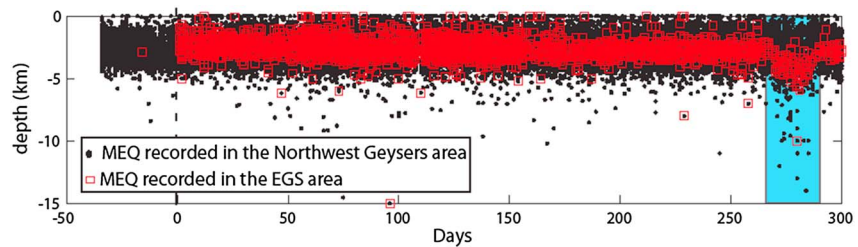
Figure 3. Microseismicity evolution: depth versus time (days after start date of injection stimulation at P32). The blue strip represent the period of 3 weeks when deepening of the hypocenters below 5 km occurred [from *Jeanne et al.*, 2014b].

on 30 November 2011. Thereafter, the injection rate was maintained at 63, 44, and 25 kg/s (1000, 700, and 400 gpm) steps for durations of 100, 105, and 35 days, respectively (Figure 2a).

3. Microseismic Activity

3.1. Volume of Injected Water Versus Microseismic Activity

Microseismicity was recorded by a dedicated seismic monitoring network deployed throughout The Geysers [*Boyle and Zoback*, 2013]. This network consisted of 31 three-component short-period stations with a sampling frequency of 500 Hz [*Majer and Peterson*, 2007]. Before injection, only one microseismic events was detected in the EGS area from 1 September 2011 to the start of injection (6 October 2011). Then, from 6 October 2011, to 11 months later (10 August 2012), about 3000 microseismic events were recorded around the P32 injection well. The event magnitudes ranged between 0.4 and 3, with only 41 seismic events having a magnitude greater than 2. After 270 days of injection, there was a period of 3 weeks when the microseismic data indicated a deepening of the hypocenters to below 5 km. This phenomenon occurred over the entire Northwest Geysers area ($\approx$90 km^2) and is believed to be related to regional tectonic activity (Figure 3) [*Jeanne et al.*, 2014b]. Therefore, we only include data up to 270 days in our study of the induced seismicity around the EGS area.

Figure 2a shows the daily evolution of the injected water volume and the number of microseismic events; Figure 2b presents the cumulative number of microseismic events as a function of the injected water volume. There appears to be good correlation between the injected water volume and the microseismic activity. The cumulative number of microseismic events increases linearly with the volume of injected water during the first 84 days of injection, after which the slope of this linear relation slightly decreases.

3.2. Spatiotemporal Evolution of the Microseismic Activity

The distribution of microseismic events is studied by using the Seismicity-Based Reservoir Characterization (SBRC) approach [*Shapiro et al.*, 1997, 2002], which links the spatiotemporal evolution of the microseismic events with the hydraulic diffusivity (D). Figure 4a is the so-called *rt* plot: it represents the distance of event locations from the injection point (*r*) versus the elapsed time (*t*) since beginning of injection. In this study, because of the high density of microseismic events the *rt* plot is also represented by a contour plot of seismic density, which shows the number of events per bin (Figure 4b). Two surfaces were defined to separate the seismically active spatial domain from the seismically quiet spatial domain: the "triggering front" following the beginning of the injection [*Shapiro et al.*, 1997] and the "back front" following the end of the injection [*Parotidis et al.*, 2004]. The appearance of these two fronts is assumed to be related to the pore pressure diffusion through the reservoir. Therefore, relationships were developed to estimate the reservoir hydraulic diffusivity in case of linear diffusion [*Shapiro et al.*, 1997] or in case of fracture opening during hydraulic stimulations [*Shapiro and Dinske*, 2009].

However, characterizing the reservoir hydraulic diffusivity from the SBRC approach can be challenging because errors in hypocenter determination can be large (from 120 to 600 m in this case) and because the triggering front is also dependent on the stress state, the coefficient of friction and the injection rate [*Schoenball et al.*, 2010]. As a result of this uncertainty, we consider the SBRC approach to describe the main characteristics of the spatiotemporal evolution of the microseismic events and to compare these features with our 3-D thermo-hydro-mechanical model. While relative changes reflect such characteristics, much less attention is given to the absolute values of hydraulic diffusivities estimated by the SBRC approach in this case.
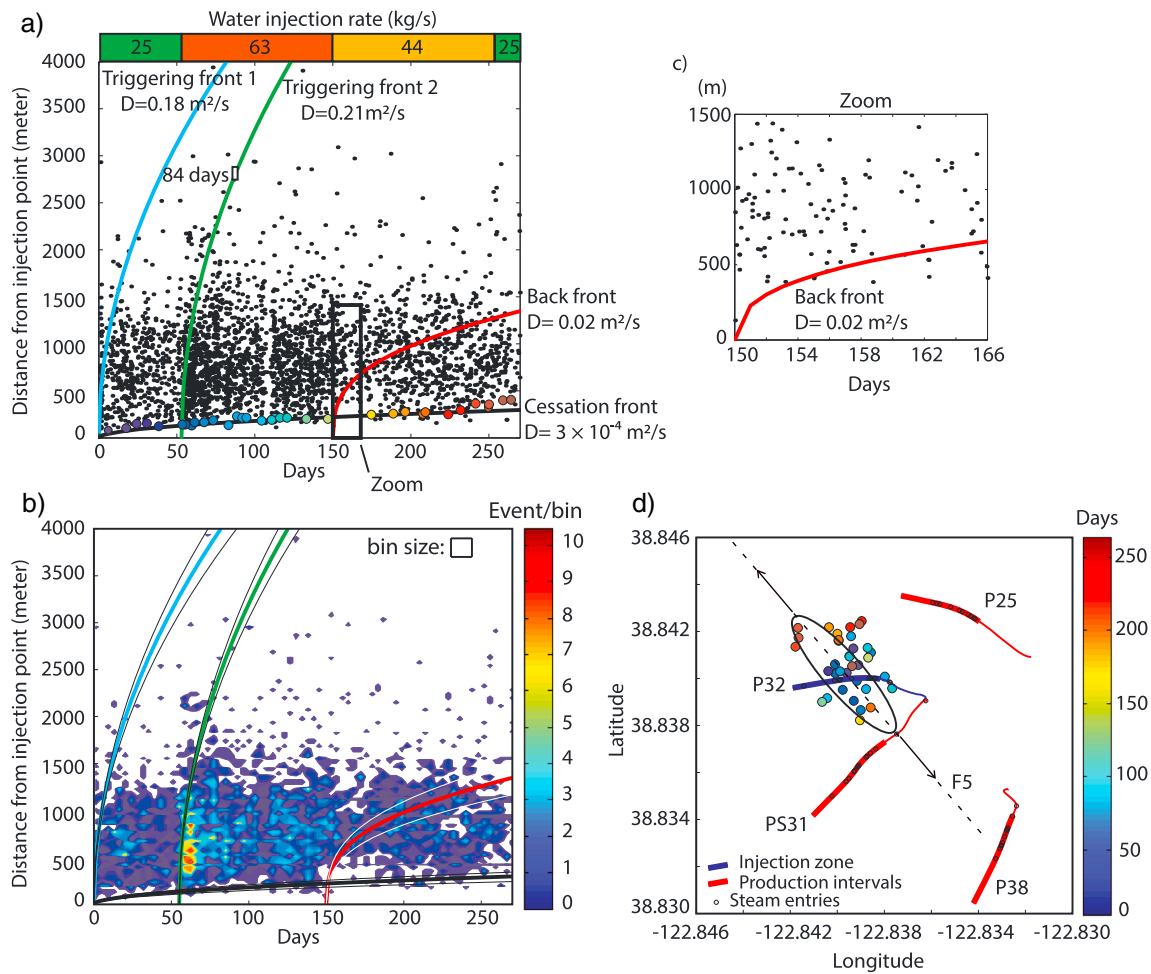
Figure 4. Characterization of microseismic activity using the Seismicity-Based Reservoir Characterization approach (a) *rt* plot of induced microseismic events, the thick lines are the triggering fronts TF1 (in blue) and TF2 (in green) calculated after an increase of the injection rate, the back front (in red) calculated after a decrease of the injection rate BF, and the cessation front (in black). (b) *rt* plot presented by a contour plot of seismic density, with the different fronts established and their uncertainty: ±0.02 m²/s for TF1 and TF2, ±0.005 m²/s for BF, and ±10−4 m²/s for the cessation front. (c) Zoom on the period during which the back front (in red) has been calculated. (d) Spatiotemporal evolution of the microseismic events located along the cessation front (colored events from Figure 4a).

As a first-order approximation, we assumed that the pore fluid pressure perturbation induced by fluid injection obeys the law of linear diffusion, because no evidence of significant fracture opening during hydraulic stimulations has been recorded. Indeed (1) during the injection, the bottom-hole pressure was kept much less than the estimated minimum principal compressive stress at injection depth, avoiding the creation of new fractures and (2) the injectivity tests showed that no apparent injectivity gain occurred during the stimulation [*Garcia et al.*, 2012; *Rutqvist et al.*, 2015]. The repeated injectivity tests showed an apparent linear relation between downhole pressure (water column) and injection rate, with no significant change in injectivity between the different injectivity tests conducted during the course of the stimulation [*Garcia et al.*, 2012]. Following the assumption of linear diffusivity, the relation linking the triggering front *rt* to the reservoir hydraulic diffusivity can be written as [*Shapiro et al.*, 1997]

$$r_t = \sqrt{4\pi D t}, \tag{1}$$

where t is the time from the injection start or the time from the increase in the injection rate.

Because the injection scheme consists of steps over several months of increasing and decreasing rates, we were able to calculate two triggering fronts (Figures 4a and 4b), with an uncertainty of ±0.02 m²/s (Figure 4b), using the assumption of linear diffusivity. The presence of a second triggering front can be attributed to the Kaiser effect. The first injection step (at 25 kg/s) creates a pressure pulse which propagates

through the reservoir inducing failure along the most critically stressed fractures. Then the increase in injection rate (almost 3 times higher than the first one: 25 to 63 kg/s) leads to the propagation of a higher-pressure pulse. A new state of stress was reached inducing failure along fractures less critically stressed. We did a sensitivity analysis on the hydraulic diffusivity to find the fronts which best separate the seismic domain from the quiet domain. The best fit was found by a visual estimation. The first triggering front corresponds to a diffusivity $D = 0.18\,\text{m}^2/\text{s}$ from the beginning of the injection when the injection rate was kept at 25 kg/s (400 gpm), and the other corresponding to a diffusivity $D = 0.21\,\text{m}^2/\text{s}$ following the increase in the injection rate to 63 kg/s (1000 gpm). These two "triggering fronts" are considered to border the seismically active and seismically quiet spatial domains. However, the second triggering front only explains the spatiotemporal evolution of the microseismic events during 1 month after the injection-rate increase (from 55 to about 84 days). Indeed, after about 84 days, the seismically active domain stops growing and reaches its biggest size, with a radius of about 3 km (Figure 4a).

We also observed a reduction in seismic activity during the two weeks following the decrease in injection rate from 63 to 44 kg/s (1000 to 700 gpm) after 150 days of injection. Because injection and (hence) microseismicity kept occurring after 150 days, it was hard to observe a back front. However, based on the 16 days immediately following the decrease in injection rate, from 63 to 44 kg/s (1000 to 700 gpm), a back front ($D = 0.02\,\text{m}^2/\text{s}$) can be discerned, separating the seismically active and quiet spatial domains (Figure 4c).

Interestingly, a seismically quiet spatial domain also appears just around the injection well. In this paper, we use the term *cessation front* to describe the surface separating the seismically quiet domain around the injection well from the surrounding (seismically active) reservoir domain (Figures 4a and 4b). Using equation (1), the cessation front diffused through the reservoir corresponding to a diffusivity of $3.0 \times 10^{-4}\,\text{m}^2/\text{s}$. To highlight how this aseismic domain developed, we studied in detail the spatiotemporal evolution of the microseismic events located along the cessation front (Figure 4a). In Figure 4a, we used different colors—blue, green, and red—to define the different fronts in the evolution of the microseismic events from the beginning of injection to 270 days, whereas Figure 4d shows the hypocenter location of these microseismic events. At the beginning of the injection, the domain around the injection well is seismically active, as shown by the presence of blue microseismic events around the injection well (Figures 4a and 4d). Then, over time, the aseismic domain grows around the injection well, which is shown by the red microseismic events located farther from the injection well (Figures 4a and 4d). The aseismic domain apparently grows along the northwest striking (N130) shear zones that intersect the injection well (Figure 1a).

4. Thermo-Hydro-Mechanical Simulation

We use the coupled THM simulator TOUGH-FLAC, described in *Rutqvist et al.* [2002] and *Rutqvist* [2011]. TOUGH-FLAC links the TOUGH2 (finite volume) multiphase flow and heat transport simulator [*Pruess et al.*, 2011], which has the ability to simulate both advection and conduction in fault and matrix blocks and all the water properties (represented by the steam table equations as given by the *International Formulation Committee* [1967]), and the FLAC3D (finite difference) geomechanical code [*Itasca*, 2009] for coupled THM analysis under multiphase flow conditions.

4.1. Fluid Pressure/Stress Coupling and Fault Instability

The rock mass is simulated as an equivalent continuum with implicit representation of fractures, whereas shear zones are explicitly represented as 15 m wide zones with different hydraulic and mechanical properties (Figure 5a). In the model, the rock mass behaves as an elastic material, whereas shear zones are governed by an elastoplastic constitutive law. In this way, shear zones are envisioned to include an intensively fractured damage zone, where fractures of any orientation could exist (Figure 1a). Such an assumption is supported by studies of fault-plane analysis of seismicity at The Geysers by *Oppenheimer* [1986], which indicate that seismic sources occur from almost randomly oriented fracture planes [*Johnson*, 2014]. The assumption is also supported by seismic source analysis of microseismic events around P32 by *Boyle and Zoback* [2013], indicating that these events occurred on subvertical fractures that are oblique to the main strike of the shear zone. Under this assumption, we used the isotropic Mohr-Coulomb model, where fractures of any orientation can be reactivated (Figure 5b). The position of a stress point on the failure envelope is controlled by a nonassociated flow rule for shear failure and an associated rule for tension failure [*Itasca*, 2009].
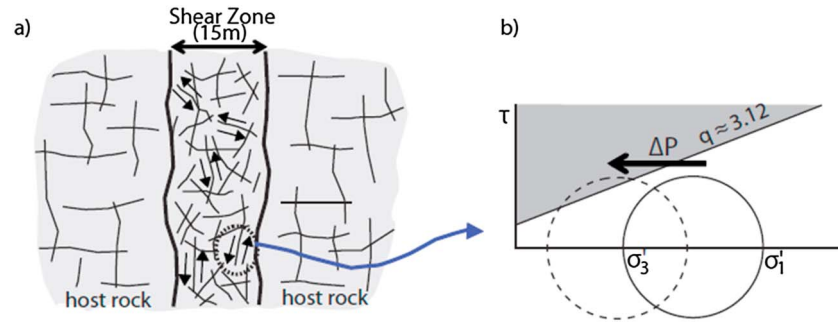
Figure 5. Illustration of the approach for failure analysis to evaluate the potential for induced seismicity within a (a) shear zone of highly fractured rock with randomly oriented fractures within the 15 m thick shear zone, and (b) movements of Mohr's circle as a result of increased fluid pressure within a fracture plane of a near critically stressed fracture and domains used in the definition of the flow rule.

According to the Mohr-Coulomb failure criterion, failure occurs when the difference between the maximum principal compressive effective stress σ'_1 and minimum compressive principal effective stress σ'_3 is sufficiently large. Considering compressive stress of a positive quantity, we define the maximum and minimum compressive effective stresses as $\sigma'_1 = \sigma_1 - \alpha P_f$ and $\sigma_3 = \sigma_3 - \alpha P_f$, where P_f is the fluid pressure and α is Biot's coefficient [*Biot*, 1941]. Assuming $\alpha = 1$, the limiting ratio of σ'_1 and σ'_3 is given by [*Jaeger and Cook*, 1979]

$$\frac{\sigma'_1}{\sigma'_3} \leq q = \left[\left(\mu^2 + 1 \right)^{1/2} + \mu \right]^2, \tag{2}$$

where q is the limiting stress difference (slope of the σ'_1 versus σ'_3 line). For our study, μ was set to 0.6, which corresponds to a q value of 3.12 (Figure 5b). $\mu = 0.6$ is a lower limit value frequently observed in studies of the correlation between active fault zones and maximum shear stress [*Byerlee*, 1978; *Sibson and Rowland*, 2003].

4.2. Mechanical Effects on Porosity and Permeability

Stress-induced changes in rock-mass permeability are notoriously difficult to predict in complex fractured rock masses [*Rutqvist and Stephansson*, 2003; *Rutqvist*, 2015]. However, laboratory investigations on single rock fractures [*Makurat et al.*, 1990; *Olsson and Barton*, 2001] and numerical studies on fractured rock mass [*Min et al.*, 2004] have shown that nonlinear deformation and shear dilation associated with the reactivation of preexisting fractures can significantly change the rock-mass permeability. Other studies have also shown that changes in permeability depend on the elastic properties of the surrounding rock mass [*Dieterich*, 1992; *Rutqvist et al.*, 2013] and on the fracture network properties [*Min et al.*, 2004; *Baghbanan and Jing*, 2008; *Koh et al.*, 2011; *Zhao et al.*, 2013]. Indeed, substantial permeability changes by shear reactivation of fractures in crystalline rock require a fracture shear displacement of several millimeters [*Rutqvist and Stephansson*, 2003]. Nonetheless, shear displacement can be limited by the fracture length [*Rutqvist*, 2015], so that fractures must be long enough or located within a highly fractured zone, like a shear zone, to allow for substantial shear-induced permeability changes [*Rutqvist*, 2015].

Under these assumptions, to simulate changes in permeability associated with the shear reactivation of the preexisting fractures within the shear zones affecting the EGS area, we choose to use a stress-permeability relation in which changes in permeability depend on the effective normal stress and on the plastic shear (pss) and tensile strain (pts). *Hsiung et al.* [2005] derived the relation between these parameters, the porosity and permeability of a fracture. Following their approach, changes in porosity caused by plastic deformation are calculated as

$$\begin{cases} \phi_{hm} = \phi_0 + \Delta\phi_{fp} \\ \Delta\phi_{fp} = e_{\text{pts}} + e_{\text{pss}} \tan \psi \end{cases} \tag{3}$$

where $\Delta\phi_p$ are the changes in porosity that depend on plastic tensile strain (e_{pts}) and plastic shear strain (e_{pss}). However, in our case the bottom-hole pressure was kept less than the estimated minimum principal compressive stress, so the plastic tensile strain (e_{pts}) is null. ψ represents the dilation angle of fractures within
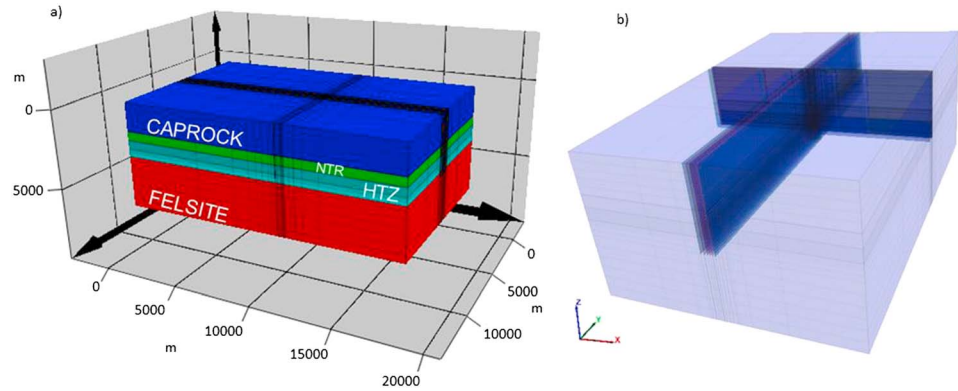
Figure 6. Three-dimensional numerical grid with (a) material layers showing the caprock (dark blue), the Normal Temperature Reservoir (NTR, green), the High Temperature Zone (HTZ, blue), and the felsite (red) and (b) fault zone network; only one member of each fault zone set is shown.

a shear zone. The permeability changes are then based on a nonlinear function of the effective stress normal across the shear zones (σ'_n), as well as depending on the plastic strain:

$$
\begin{cases}
\kappa_{hm} = \kappa_0 \left[\dfrac{a}{c(c\sigma'_n + 1)} \sqrt{\dfrac{\phi_0}{12\kappa_0}} + \dfrac{e_{pts} + e_{pss} \tan \psi}{\phi_0} \right]^3 \\[2em]
a = K^{-1} \\[1em]
c = \dfrac{-1 \pm \sqrt{1 + 4\sigma'_n a \sqrt{\dfrac{\phi_0}{12\kappa_0}}}}{2\sigma'_{n0}}
\end{cases}
\tag{4}
$$

where a and c are two empirical constants for describing the normal-closure hyperbola [*Bandis et al.*, 1983] that can be approximated from the limiting fracture normal stiffness (K) at zero effective normal stress and from the initial normal effective stress (σ'_{n0}).

This stress-permeability relation was originally developed to study changes in permeability in a rock mass composed of one set of fractures [*Hsiung et al.*, 2005]. Here because shear zones are viewed as highly fractured with randomly oriented fractures, we focus our analysis on the global THM behavior of the shear zone. Consequently, we used the effective normal stress acting on the shear zones, a global initial stiffness ($K = 15$ GPa), and a global dilation angle of 1° (These parameters are discussed in the section 5.4.)

4.3. Model Geometry

The 3-D numerical model represents the study area associated with the Northwest Geysers EGS Demonstration Project. This model is fully described in *Jeanne et al.* [2014c]. Geometric configuration of the shear zone network and the wells in this area are shown in Figure 1. The numerical model extends vertically from 0 to 6500 m in depth and 20 by 12 km horizontally. We discretize the model by rectangular elements. The smallest elements (15 m × 50 m × 50 m) are found within the shear zone inside the EGS area. Farther from the injection zone, the mesh spacing increases progressively toward the model boundaries. The high mesh resolution close to the injection well allows us to better capture the formation, the shape, and the size of the liquid saturated area around the well. Inversely, far from the EGS area, the coarse mesh increases the uncertainty on the size of the stimulation zone; however, the uncertainty stays low (up to 100–200 m). This simplified model consists of four layers: a graywacke-dominated caprock, a normal temperature (240°C) reservoir (NTR), a high-temperature zone (HTZ), and a granite intrusive (felsite) layer [*Garcia et al.*, 2012] (Figure 6). Eleven shear zones are represented: eight trending N130 and three trending N050 (Figure 1c).

The simulated wells are made of two parts (Figure 1d): an upper encased vertical zone where no fluid flow and no heat exchange are allowed with the surrounding rock, and the deeper injection or production zones, where heat and flow communication are allowed with the reservoir. These zones are curved to have
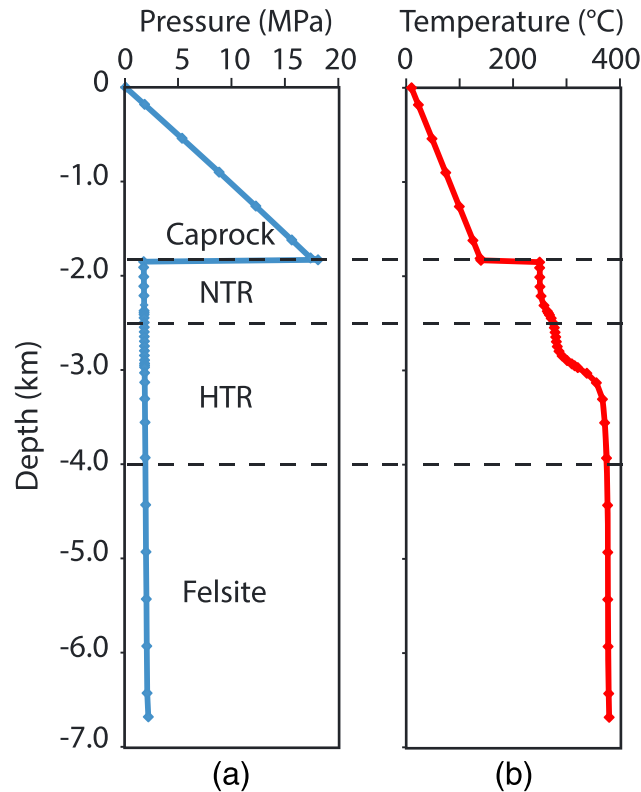
Figure 7. Initial conditions: (a) pressure and (b) temperature gradient.

the same trajectory as that of the wells in the field. Water was injected at 90°C in the simulations, which results in a downhole fluid injection temperature of 90°C at the bottom of an internal well liner.

4.4. Initial and Boundary Conditions

The initial thermal and hydrological conditions (vertical distributions of temperature, pressure, and liquid saturation) were established through steady state, multiphase flow simulations [*Rutqvist et al.*, 2015].The initial reservoir temperature in the NTR is ~240°C down to a depth of about 2.5 km and then gradually increases up to 370°C toward the bottom boundary at a depth of 6.5 km (This lower value than the measured 400°C was used because it is the upper temperature limit of the TOUGH module used). At The Geysers, the steam pressure within the hydraulically confined NTR has gradually decreased with steam production since the 1960s and is today a few
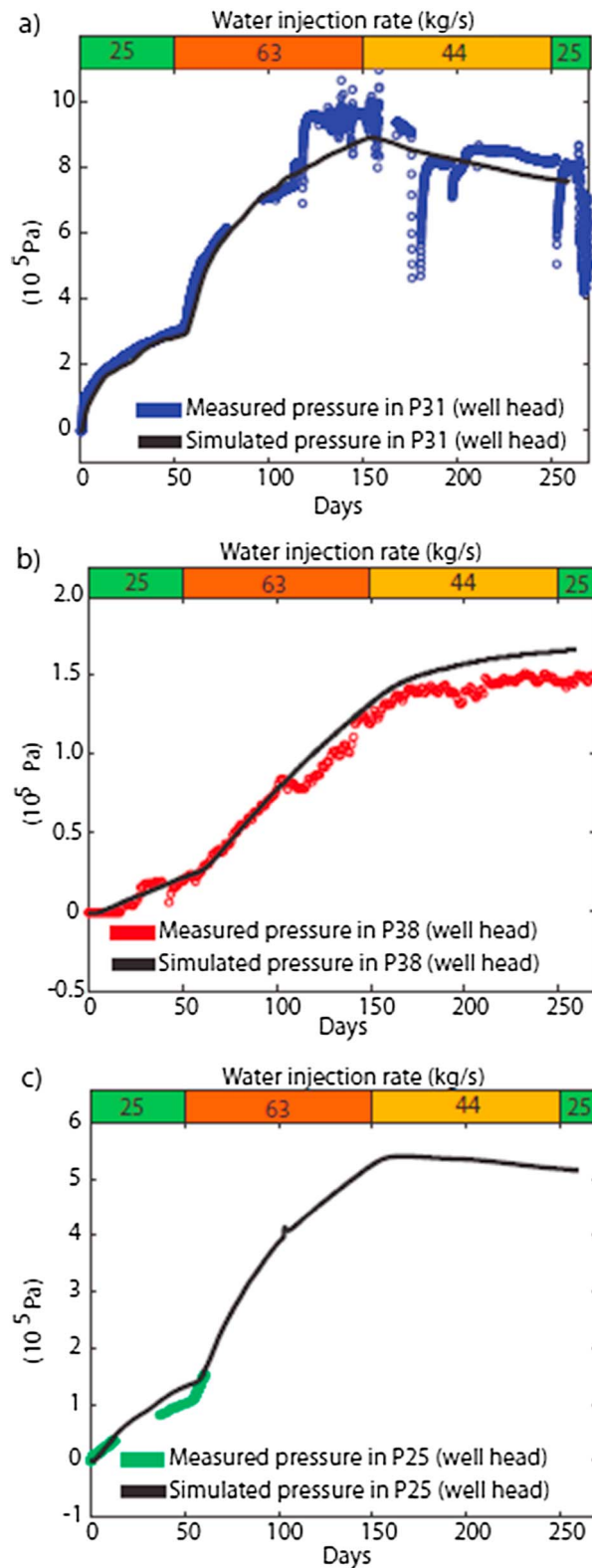
megapascals (≈ 2 MPa), whereas the pressure outside the sealed reservoir is hydrostatic. Thus, the initial reservoir pressure in the model simulations related to the new EGS and injection is a few megapascals (≈ 2 MPa) (Figure 7). To simulate such initial conditions, a very low permeability at base of the caprock is needed. Null displacement was imposed on the bottom and side boundaries, whereas the top boundary is free to move. Open flow boundaries were imposed on all model boundaries (i.e., constant pressure and temperature).

4.5. Mechanical and Thermal Properties and In Situ Stress Field

The values of the Young's modulus of the rock mass ($E = 28$ GPa) and the shear zones (E = 15 GPa) used in our simulation were estimated by fitting the simulated ground surface deformations with displacement time series measured from satellite, with a Poisson ratio equal to 0.25 [*Jeanne et al.*, 2014c]. The linear thermal expansion coefficient of the rock (α_t), the thermal conductivity, and the specific heat were set to 1×10^{-5}°C^{-1}, 4.2 W/m°C, and 880 J/kg°C, respectively, corresponding to values determined from core samples of the reservoir rock at high (250°C) temperature [*Mossop and Segall*, 1997]. In the simulation, an initial in situ stress regime was imposed consistent with the dominant crustal transtensional stress regime at The Geysers [*Oppenheimer*, 1986; *Stark*, 2003]. Studies of earthquake focal plane mechanisms indicate that the maximum principal horizontal stress ($S_{Hmax} = \sigma_2$) is oriented N020E [*Boyle and Zoback*, 2013], and it is approximately equal to lithostatic (or vertical) stress S_v (which is equal to σ_1) [*Boyle and Zoback*, 2013; *Oppenheimer*, 1986]. To estimate the value of the least principal horizontal stress ($S_{Hmin} = \sigma_3$), *Jeanne et al.* [2014c] performed a sensitivity analyses to match the shear zone mechanical elastoplastic response with observed induced seismicity. The best fit was obtained with $\sigma_3 = 0.341 \times \sigma_1$ while assuming $\sigma_2 = 0.9 \times \sigma_1$.

4.6. Initial Hydraulic Properties and Parameters for the Stress-Permeability Relation

The hydraulic properties for the NTR and the caprock are equivalent to those used in *Rutqvist et al.* [2015] and are parameter values originally derived from standard reservoir models of The Geysers geothermal field. On the other hand, the hydraulic properties of the HTR and the shear zones were estimated during a sensitivity

Figure 8. Comparison between the pressure evolutions measured in situ in wells (a) PS31, (b) P38, and (c) P25, with the calculated pressure evolution. Note that the pressure monitoring for P25 was limited to the time before the well was placed into production and the difference in scales used on the pressure axes.

analysis by using multiphase fluid flow analysis with TOUGH2 and the EOS3 fluid equation of state [*Pruess et al.*, 2011]. The initial permeability and porosity were estimated by matching the monitored well-head pressure variations in three wells around the injection well: PS31, P38, and P25 (Figure 8). The initial permeabilities are given in Table 1. These results are slightly different from *Jeanne et al.* [2014c], because in *Jeanne et al.* [2014c] no changes in permeability were considered to match the monitored well-head pressure variations—unlike here.

Shear zones are simulated with an isotropic Mohr-Coulomb model, which implies that fractures of any orientation exist and could be reactivated. Nonetheless, we use a stress-permeability relation originally developed to study changes in permeability in a rock mass composed of one set of fractures. Because of this difference, we need to verify if the parameters used in the stress-permeability relation are reasonable. To discuss this, we use shear zone F5 as an example.

4.6.1. Initial Permeability and Porosity

From the sensitivity analysis, the estimated F5 permeability (k) and porosity (ϕ_f) are equal to $2.4 \times 10^{-14}\,\mathrm{m}^2$ and 3% (Table 1). With these properties, and assuming that the rock mass is composed of one set of fractures, we can calculate the initial aperture from the cubic relation between fracture flow and aperture (equation (5)) and then the fracture density (equation (6)).

$$b = \sqrt{\frac{12k}{\phi f}} \qquad (5)$$

$$b = \frac{\phi f}{f d}, \qquad (6)$$

where "b" is the fracture aperture and "f_d" is the fracture density. We find an initial aperture of $3.6 \times 10^{-6}\,\mathrm{m}$ and a fracture density equal to 9682 fractures per meter, which is not reasonable. It is difficult to estimate the fracture spacing inside a shear zone because there are many fractures, and a few of them may dominate flow. Also, equation (5) is

Table 1. Material Properties Used During the Simulation

	Shear Zones													
	F1	F2	F3	F4	F5	F6	F7	F8	Fa	Fb	Fc	NTR	HTR	Felsite
Permeability (m2)	1.0E-14	8.0E-14	6.0E-14	4.0E-14	2.4E-14	1.0E-14	6.0E-16	6.0E-16	5.0E-15	5.0E-15	1.0E-20	5.0E-14	1.0E-16	1.0E-16
Porosity (%)	3.0	3.0	3.0	3.0	3.0	3.0	3.0	3.0	1.0	1.0	1.0	2.0	2.0	2.0

highly idealized, assuming flow in isolated parallel plate fractures, whereas the porosity we may evaluate from cross-hole tests includes flow storage along the flow path, which may be substantially higher than the porosity provided by the isolated flow path aperture. While the permeability may be dominated by the flow along the fractures, there is substantial fluid storage capacity provided by the rock matrix adjacent to the fracture, perhaps connected to the main fracture by numerous microfractures and damaged rock. Therefore, to better describe the shear zones and their hydraulic behavior, we need to consider using two porosity values: (1) one representing the flow storage that affects the pressure diffusion within the shear zones (in this case, we use the porosity value obtained during the sensitivity analysis) and (2) another corresponding to the set of parallel fractures used for calculating mechanically induced permeability changes. Because intersections between wells and shear zones are characterized by the presence of clustered steam entries about 15 to 30 m wide, it is reasonable to assume fracture spacing on the order of meters for fractures providing the dominant flow paths along the shear zones. Under this consideration, $f_d = 1$ and $k = 2.4 \times 10^{-14}$ m^2 correspond to a theoretical parallel plate fracture porosity of 6.6×10^{-3}% for the shear zone F5 (equations (5) and (6)). This value is used in equations (3) and (4) to calculate changes in permeability during the simulation, whereas the 3% porosity value listed in Table 1 is the actual value used for fluid storage in the shear zones.

4.6.2. Initial Fracture Normal Stiffness

Figure 9a presents rock-mass permeability as a function of effective normal stress when considering initial fracture normal stiffness values of 1.5, 15, and 150 GPa/m. These three curves are calculated by using equation (4), by considering plastic shear (e_{pss}) and tensile strain (e_{pts}) as null, and by assuming an initial effective normal stress (of 60 MPa) at the depth of the injection. We observe that when the effective normal stress is higher than 50 MPa, changes in initial stiffness over 2 orders of magnitude do not have a significant impact on the stress-permeability relation. In the present case, at The Geysers, the initial reservoir pressure is a few megapascals (≈ 2 MPa); and consequently, the effective normal stress at the depth of the injection is very high (close to 60 MPa). Thus, according to Figure 9a, the assumed initial fracture normal stiffness will not have a significant impact on our results. However, an initial normal stiffness equal to 15 GPa/m seems reasonable when looking at the relation between fracture aperture and effective normal stress (equation (7)) [Hsiung et al., 2005] with a maximum aperture of about 0.6 mm (Figure 9b).

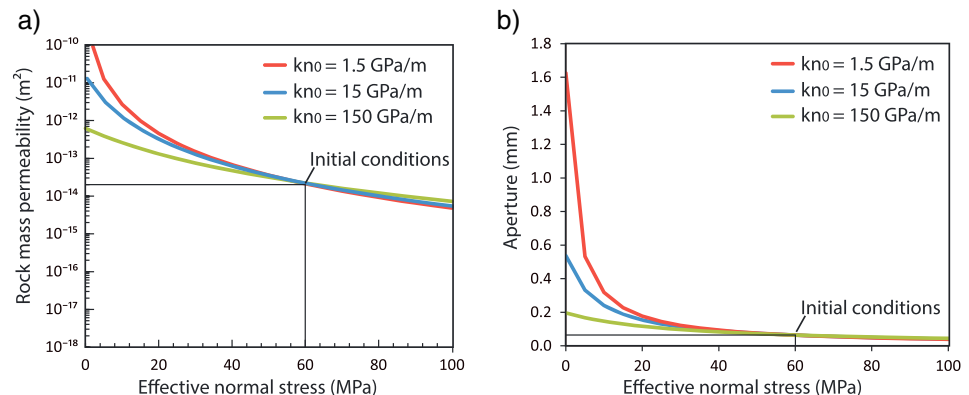$$b = \frac{a}{c(c\sigma_n + 1)} + \frac{e_{pts} + e_{pss}\tan\psi_f}{fd} \tag{7}$$

Figure 9. Influence of initial normal stiffness on (a) rock-mass permeability and (b) fracture apertures.
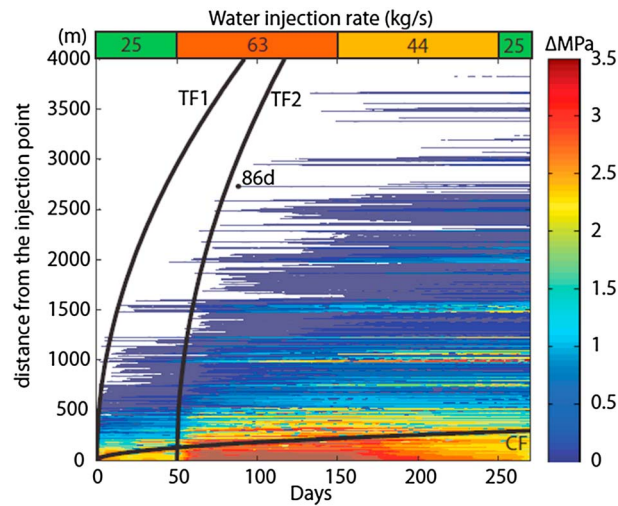
Figure 10. Comparison between the evolution of the pressure distribution through the reservoir over time with the triggering fronts TF1 (blue) and TF2 (green) and the cessation front CF (black) estimated from the *rt* plot.

The relation between stress, rockmass permeability, and hydraulic conducting fracture aperture are not unrealistic in comparison with such relation derived from field data at several sites, as presented in *Rutqvist* [2015].

4.6.3. Dilation Angle

It is known that The Geysers geothermal reservoir is near critically stressed for shear activation [*Lockner et al.*, 1982; *Oppenheimer*, 1986; *Rutqvist et al.*, 2015]. The reservoir is being subjected to a regional strain that would be expected to cause slow shear straining along regional faults and could also reactivate smaller preexisting fractures, perhaps aseismically, including creep. The fact that a permeable geothermal reservoir exists at The Geysers would indicate that such shear activation takes place over geologic time. For example, during a few weeks at the end of 2012, deeper than normal microseismic activity within the Northwest Geysers area was believed to be related to regional tectonic activity [*Jeanne et al.*, 2014b]. This means that fractures in this area could have already been dilated by shear in the past. This might be especially true for shear zones often associated with a cluster of steam-bearing fractures intersecting wells. Additional shear may not cause significantly more opening. Thus, the dilation angle would be more or less 0, and there would not be much aperture change resulting from additional shear. Moreover, the estimated stress normal to fracture planes is very high (over 60 MPa), which means that shearing would likely lead to breaking of fracture surface asperities rather than allowing the fractures to dilate. Under these assumptions, we start the simulation with a low dilation angle equal to 1°. (This value is discussed below.)

5. Comparison Between Microseismic Activity and THM Modeling

5.1. Pressure Diffusion Versus Seismic Deformation

Every 10 days, in each cell of the model, the calculated pressure variation was extracted. In this way, we are able to present, in Figure 10, the pressure diffusion through the model from the injection point versus the elapsed time since beginning of injection. Areas with pressure variations lower than 0.06 MPa are in white. During the first weeks of injection and the weeks following the increase in the injection rate from 25 to 63 kg/s (400 to 1000 gpm), the surfaces bounding the spatial domain where the pore pressure increases occur match the triggering fronts 1 and 2 previously identified in the *rt* plot. Also, after ~86 days of injection, the pore pressure diffusion deviates from triggering front 2, similar to what was observed in the *rt* plot. During the rest of the injection period, the pore pressure front stabilizes at about 2700 m from the injection well. These observations confirm that the pore pressure diffusion through the reservoir is the main mechanism of induced seismicity away from the injection well. Also, the change in the slope of the correlation between the cumulative number of microseismic events and the volume of injected water (Figure 2b) seems to occur when the pore pressure pulse ceases to expand (after ~86 days in our simulation). At that time, it seems that the pore pressure increase along the triggering front became too low to trigger microseismicity; hence, the rate of microseismicity decreased.

5.2. Temperature Diffusion Versus Aseismic Deformation

We have studied in detail the THM behavior of shear zone F5, where an aseismic zone seems to develop during the injection (Figure 4d). Figure 11 presents the temperature evolution within F5. Interestingly, it appears that the surface bounding the spatial domain where the temperature decreased matches the cessation front established in the *rt* plot (Figure 4a).
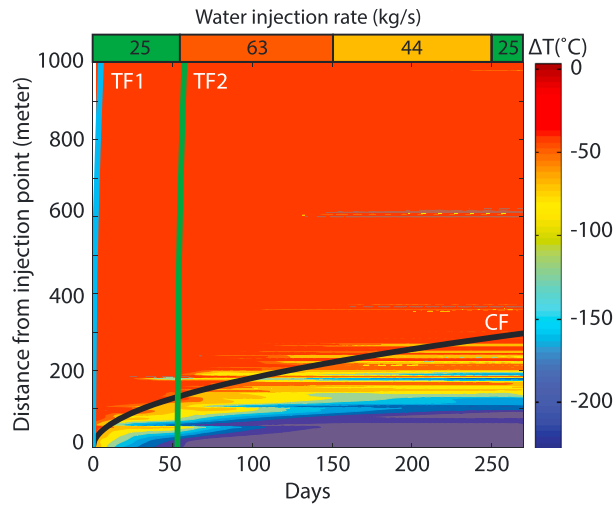
Figure 11. Comparison between the temperature distributions within the shear zone F5 over time with the triggering fronts TF1 (blue) and TF2 (green) and the cessation front CF (black) estimated from the *rt* plot.

We also studied the stability of the shear zone F5 during injection. Every 10 days and in each cell of the shear zone F5, we calculated the σ'_1/σ'_3 ratio to see if the failure criterion was reached ($\sigma'_1 = 3.12 \times \sigma'_3$). Results are presented in Figure 12, with red cells indicating where the critical σ'_1/σ'_3 ratio is reached, and blue cells where there is no rupture. It appears that the surface bounding the spatial domain, where the stress state indicates active failure (red in Figure 12) from the spatial domain where the failure criterion is not reached (blue in Figure 12), matches the cessation front during the first 150 days and then matches the back front from 150 to 270 days.

The thermo-mechanical processes responsible for suppressing microseismic activity have been described in detail by *Jeanne et al.* [2014c]. These processes are presented in Figure 13, where we compare the evolution of pressure, temperature, stresses, and shear zone stability calculated at one control point, located inside the seismically quiet domain (at 50 m from the injection well), with the evolution of those parameters at another control point within the surrounding seismically active domain (at 350 m from the injection well).

1. *At 50 m from the injection well*. During the first 24 h of injection, the high initial rate (60–65 kg/s) caused a significant increase in pressure, the σ'_1/σ'_3 ratio reaches the failure criterion ($\sigma'_1 = 3.12 \times \sigma'_3$), and rupture occurs. This is consistent with the microseismic activity recorded during the day following the injection (Figure 4). Then, after a few days of injection, the liquid zone reaches the first control point (50 m away from the injection well) and the temperature at this point drops from 320°C to 270°C (Figure 13a). This cooling causes a contraction of the reservoir, which has a strong impact on the local stress state, and σ_1 and σ_3 decrease (Figure 13b). Because gravity flow is predominant, the vertical stress (here σ_1) decreases much more than the horizontal stress σ_3: after 10 days of injection σ_1 and σ_3 have decreased by 12.6 MPa and 2.4 MPa, respectively. The main consequence is that the σ_1/σ_3 ratio decreases (Figure 13c), so the shear zone becomes less critically stressed and the rupture stops. The pressure increase causes reservoir expansion, creating poroelastic compressive stress that is transferred inside the reservoir. In the cooling area, the compressive stress propagates more in the σ_1 direction than in the σ_3 direction, leading to an increase in the σ_1/σ_3 ratio. However, this increase is only visible when the temperature is quasi-constant (from 10 to 50 days and from 150

● Part of the shear zone F5 where the failure criterion is not reached (q<3.12)
● Part of the shear zone F5 where the failure criterion is reached (q=3.12)
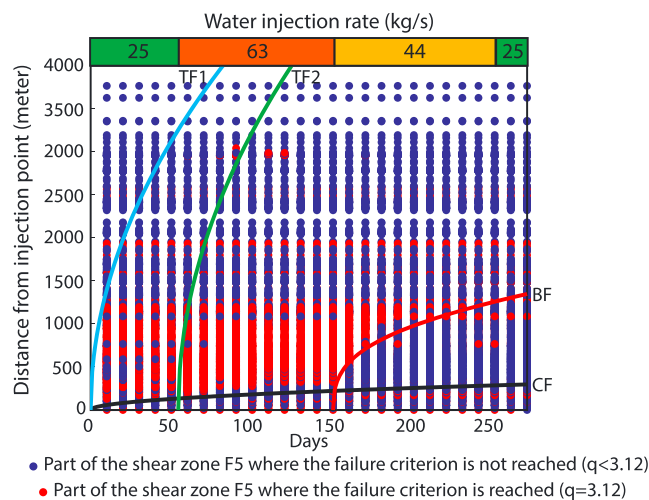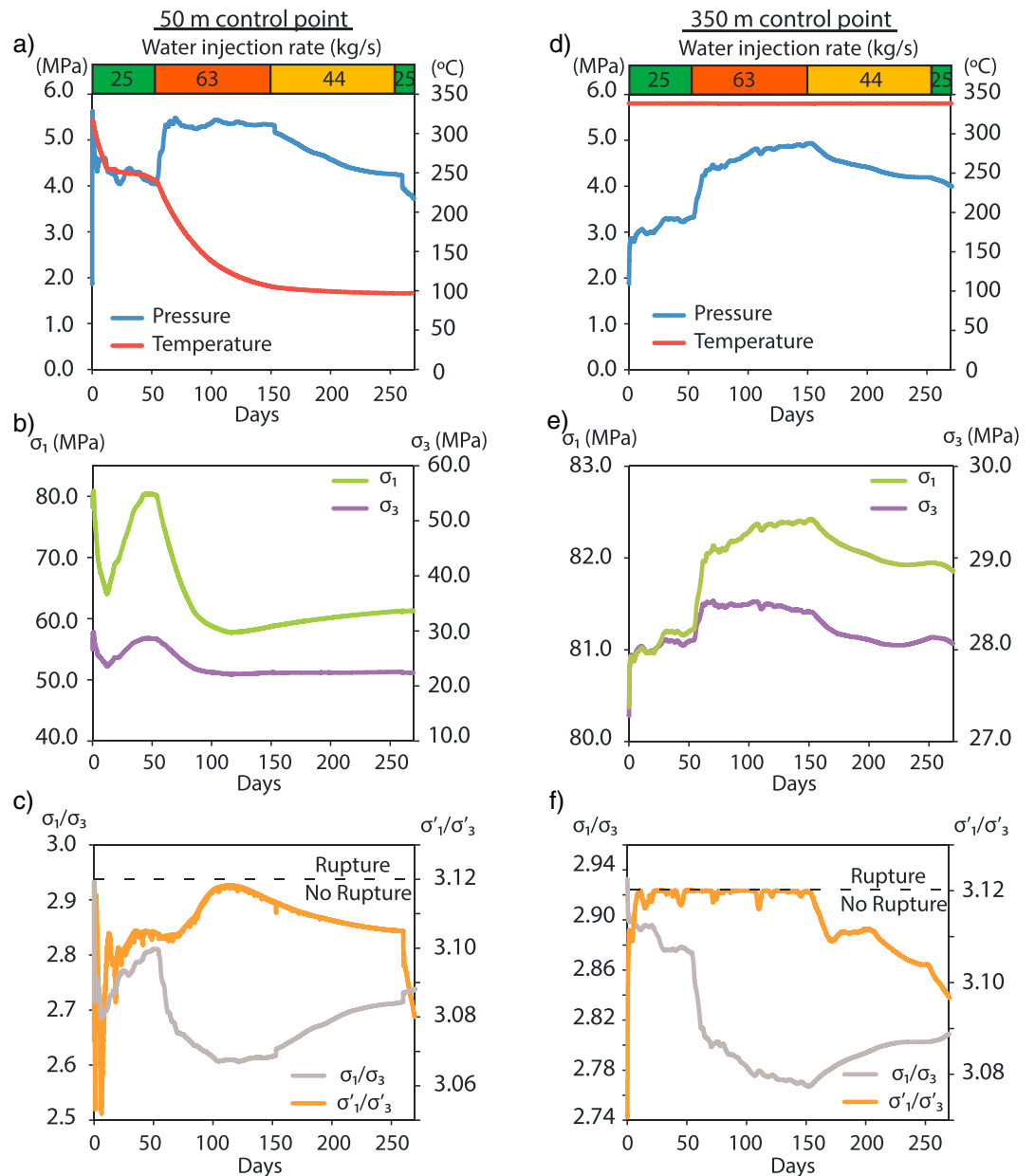
Figure 12. Comparison between the evolution of the shear zone F5 stability calculated during the THM simulation over time with the triggering fronts TF1 (blue) and TF2 (green), the cessation front CF (black), and the back front BF (red) estimated in the *rt* plot.

Figure 13. Calculated evolution of (a and d) fluid pressure and temperature, (b and e) σ_1 and σ_3, and the (c and f) ratios σ_1/σ_3 and σ'_1/σ'_3 at two control points located within the shear zone F5: A control point 50 m from the injection well located within the aseismic domain and a control point 350 m from the injection well in the seismic domain.

to 270 days), and it is not sufficient to induce shear zone reactivation. Then, the increase in injection rate from 25 to 63 kg/s (400 to 1000 gpm) results in a strong decrease in temperature, from 270°C to 100°C, after 150 days of injection, and from 100°C to 90°C during the rest of injection. Again, this temperature drop leads to a σ_1/σ_3 ratio decrease. The shear zone becomes less critically stressed and, despite the pressure increase, the shear zone is not reactivated (except during a few days after 120 days of injection).

2. *At 350 m from the injection point.* Similar to what occurs at 50 m, at 350 m from the injection point, the injection-induced pressure increase (at the beginning of the simulation) causes the stress state to reach the failure criterion ($\sigma'_1 = 3.12 \times \sigma'_3$). From that moment, a few days into the injection, shear reactivation occurs. At 350 m the pressure increase is close to what is observed at 50 m, but here there is no significant
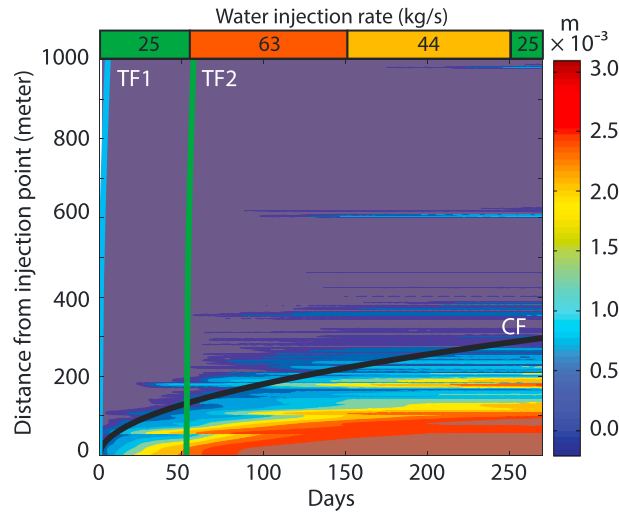
Figure 14. Comparison between the total plastic shear strain distribution along the shear zone F5 with the triggering fronts TF1 (blue) and TF2 (green) and the cessation front CF (black) estimated from the *rt* plot.

change in temperature and therefore no local cooling shrinkage influencing the state of stress. The poroelastic compressive stresses due to the reservoir expansion lead to a decrease in σ_1/σ_3 ratio but not enough to prevent the rupture. Under these conditions, the shear reactivation occurs continuously at the 350 m control point during the first 150 days of injection (Figure 13f).

5.3. Distribution of the Plastic Shear Strains Along Shear Zone F5

Figure 14 presents the distribution of the total plastic shear strains along the shear zone F5 during the injection. Note that, in our simulation, most of the shear strain is located below the cessation front in the seismically quiet domain, where the temperature drops. As seen previously, in this domain the reactivation of preexisting fractures occurs shortly after the beginning of injection, from the increase in pressure, and then the failure stops when the temperature starts dropping. In addition, our results suggest that the plastic shear strains occurring during the postfailure part inside the cooling area are much more significant than during the rupture itself.

5.4. Permeability Variations Along the Shear Zone F5

Figure 15 presents the evolution of the change factor K_{hm}/K_i (where K_i is the initial permeability) along the shear zone F5 during injection. It appears that the largest changes in permeability occur close to the injection well, in the aseismic domain of the reservoir (below the cessation front), where changes in temperature are observed.

The factors responsible for the changes in permeability are shown at the two control points, one located inside the seismically quiet domain (at 50 m from the injection well) and one located inside the seismically active domain (at 350 m from the injection well), as presented in Figure 16.
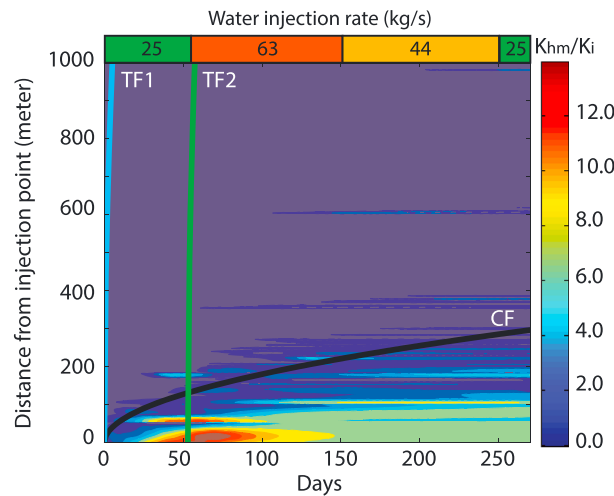
1. *At 50 m from the injection well*. In the cooling area, the permeability (Figure 16a) evolves proportionally to the evolution of the effective normal stress acting on the shear zone (Figure 16c). In general, the cooling causes a contraction of the reservoir, which tends to decrease the normal stress acting on the shear zone (Figure 16c), which favors opening of fractures and increases the overall shear zone permeability. Interestingly, we observed that despite the significant amount of plastic shear strain occurring at this point, plastic shear strain does not appear to significantly impact permeability. We also notice that the plastic shear strain inversely follows the temperature evolution
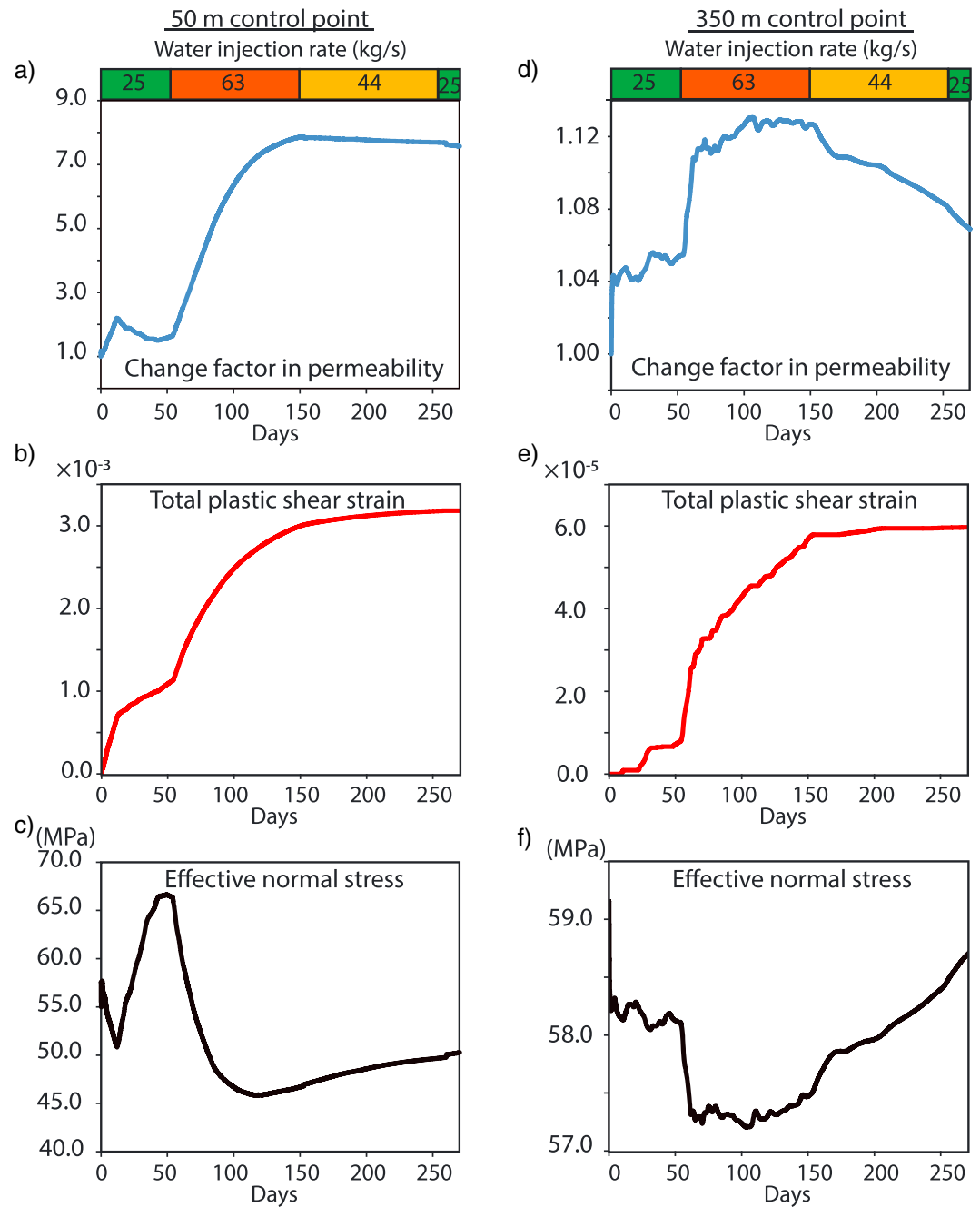

Figure 15. Comparison between the evolution of the change factor between K_{hm}/K_i along the shear zone F5 during the injection with the triggering front TF1 (blue) and TF2 (green) and the cessation front CF (black) estimated from the *rt* plot.

Figure 16. Calculated evolution of (a and d) change in permeability, (b and e) total plastic shear strain, and the (c and f) effective normal stress at two control points located within the shear zone F5: at 50 m from injection well in the aseismic domain and at 350 m from injection well in the seismic domain. Note large difference in axis scales for the two sets of plots.

(Figure 13a). In fact, below the cessation front, the relation between plastic shear strain and changes in temperature is close to pss ≈ $\alpha_t \times \Delta T$ (Figure 17). The shearing-strain increment increases due to angular distortion of rock pieces between fractures inside a heavily fractured zone.

2. *At 350 m from the injection well.* In the seismic domain, the permeability (Figure 16d) also evolves according to the evolution of the effective normal stress acting on the shear zone. The pressure increase causes a decrease in the effective normal stress, resulting in a small increase in permeability. In our simulation, the plastic shear strains at 350 m are very small and have little impact on the permeability variations. This observation is consistent with the apparent lack of injectivity gain.
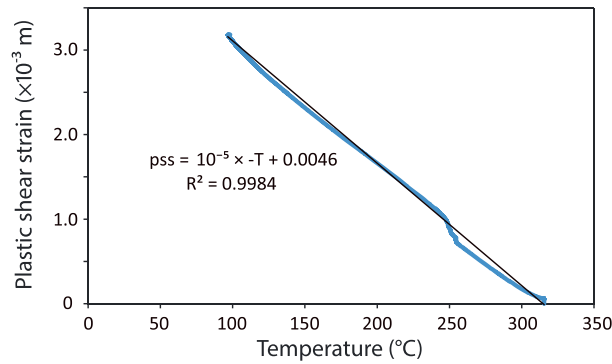
Figure 17. Relation between the plastic shear strain and the temperature calculated at 50 m from the injection well.

We investigated the effect of fault dilation angle on changes in permeability, with $\psi = 0°$, 1°, 2°, 5° and 10°, using equation (4) and the plastic shear strain calculated at 50 m from the injection well within the shear zone F5 after 270 days of injection (Figure 16). We observe that shear-induced permeability enhancement could range from 1 (with $\psi = 1°$) to 3 orders of magnitude (with $\psi = 10°$). The injectivity tests around P32 did not show significant enhancement, and it is very unlikely that the permeability could have increased by 3 orders of magnitude during the reservoir stimulation. These observations reinforce our hypothesis that the dilation angle of fractures within the shear zones at this depth may be close to zero (Figure 18).

Previously, in the *rt* plot, we highlighted an increase in hydraulic diffusivity from 0.18 m²/s at the beginning of the injection to 0.21 m²/s, ~80 days later. To compare this increase with our simulation, we considered that most of the changes in hydraulic properties occurred along shear zone F5, and we used the following equation: $D = (k*e)/S$, where k, S, and e are the permeability, the storativity, and the thickness of shear zone F5, respectively. We made the assumption that the variations in e and S are negligible compared to the changes in K. In this way, by using an initial permeability of 2.4×10^{-14} m² (derived from our sensitivity analysis) and an initial hydraulic diffusivity of 0.18 m²/s along F5, we can estimate that for a hydraulic diffusivity of 0.21 m²/s, the corresponding permeability must be equal to 2.8×10^{-14} m². Then because (from the numerical simulation) we know the volume of each cell forming shear zone F5 and the changes in permeability occurring in these cells, we are able to calculate an average permeability for a certain volume (centered on the injection point) of shear zone F5 at a certain time (Figure 19a).

Figure 19b presents the average permeability versus the considered volume of shear zone F5. We also added (within the figure) the distance between the injection point and the boundary of the considered volume (Figure 19b). This relation was established from the distribution of the permeability along F5 at 80 days of injection. We looked at the permeability at 80 days of injection, because the hydraulic diffusivity $D = 0.21$ m²/s was estimated from the triggered front TF2, which was established from 50 to about 80 days after the beginning of the injection. Globally, when we consider a larger volume of F5, its average permeability is very close to the initial permeability, and when the volume is smaller, its average permeability is higher. We found an average permeability equal to 2.8×10^{-14} m² (as the permeability analytically evaluated from TF2) for a volume extending up to 1212 m for the injection point. This value seems to be in accordance with the field observations: indeed, during the injection, most of the seismic activity (and therefore the changes in permeability) occurred in an area extending up to about 1.5 km from the injection point.
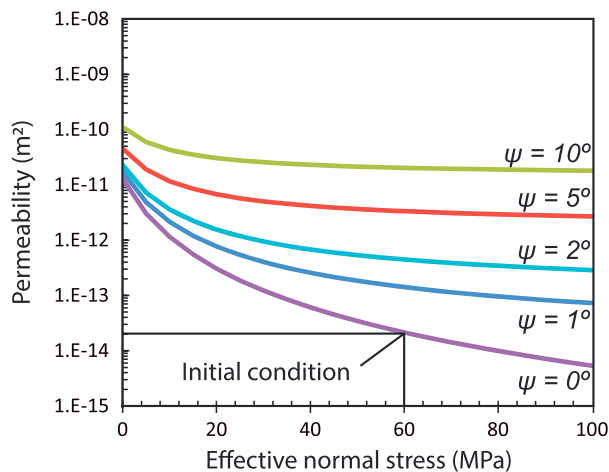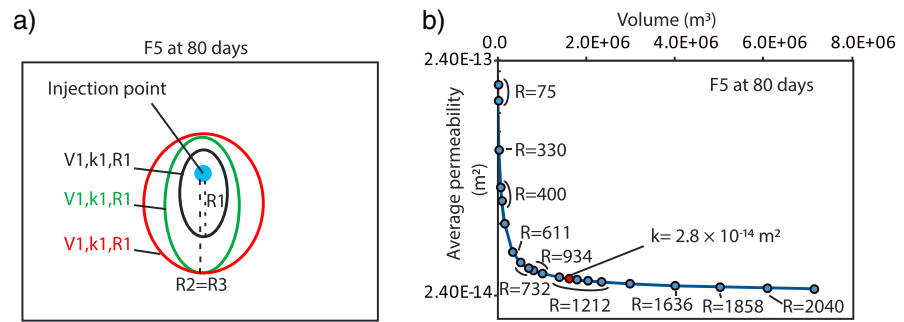

Figure 18. Influence of dilation angle of fractures within a shear zone on changes in permeability for the plastic shear strain induced 50 m from the injection well.

Figure 19. (a) Conceptual sketch of the approach used to define the permeability (*K*) of a considered volume (*V*) and its maximal extension relative to the injection point (*R*). (b) Relation between permeability and the considered volume along the shear zone F5 after 80 days of injection—the red point represents the permeability determined with the *rt* plot.

6. Conclusions

One of the most important and challenging tasks involved in the exploitation of a geothermal field is to identify where the injected water flows and where the most significant changes in reservoir properties occur. Understanding the spatiotemporal dynamics of microseismicity can greatly contribute to answering these questions. In this study, where injection occurred in an initially highly fractured, hot reservoir, we were able to distinguish a seismic and an aseismic domain around the injection well.

In the seismic domain, microseismicity is caused by the reactivation of preexisting fractures, resulting from an injection-induced pressure increase. This process occurred at a very large scale (as far as 3 km from the injection well). The change in the slope of the correlation between the cumulative number of microseismic events and the volume of injected water occurs when the expansion of the pore pressure pulse ceases to be high enough to induce microseismic events. Such information could be useful in monitoring the stimulation and evolution of an EGS in real time and knowing when the stimulated zone reaches its largest size. In our simulation, the reactivation of preexisting fractures located within a shear zone appears to have minimal impact on its permeability. The initial permeability of the shear zones is already high (up to 2 orders of magnitude higher than the host rock). On the other hand, we can suppose that the reactivation of preexisting fractures located in the host rock, where the initial permeability is very low, results in a higher gain in permeability.

In the aseismic domain, the lack of microseismic activity coincides with the presence of the injected cold water. Plastic deformations are caused by cooling contraction and by angular distortion occurring within a heavily fractured zone. They cause a cooling-stress reduction, which is higher in the direction of the water flow. In our simulations, the gravity flow causes a strong decrease in the vertical stress (here σ_1) as a result of cooling contraction, and the σ_1/σ_3 ratio decreased, which prevent shear reactivation. However, the cooling contraction of the rock leads to a decrease in the fracture normal stress favoring the fracture opening, and thus an increase in permeability. This process is localized around the injection well (up to 300 m after 270 days of injection), but it is where the most substantial gains in permeability occur.

References

Baisch, S., M. Bohnhoff, L. Ceranna, Y. Tu, and H.-P. Harjes (2002), Probing the crust to 9 km depth: Fluid-injection experiments and induced seismicity at the KTB Superdeep Drilling Hole, Germany, *Bull. Seismol. Soc. Am.*, *92*, 2369–2380.

Baghbanan, A., and L. Jing (2008), Stress effects on permeability in fractured rock masses with correlated fracture length and aperture, *Int. J. Rock Mech. Min. Sci.*, *45*, 1320–34.

Bandis, S. C., A. C. Lumsden, and N. R. Barton (1983), Fundamentals of rock joint deformation, *Int. J. Rock Mech. Min. Sci. Geomech. Abstr.*, *20*(6), 249–368.

Biot, M. A. (1941), General theory of three-dimensional consolidation, *J. Appl. Phys.*, *12*, 155–164, doi:10.1063/1.1712886.

Boyle, K., and M. Zoback (2013), Stress and fracture orientation in the northwest Geysers geothermal field, Proceedings, 38th Workshop on Geothermal Reservoir Engineering, Stanford Univ., Stanford, Calif., 11–13 Feb.

Byerlee, J. D. (1978), Friction of rocks, *Pure Appl. Geophys.*, *116*, 615–626, doi:10.1007/BF00876528.

Cornet, F. H., and O. Scotti (1993), Analysis of induced seismicity for fault zone identification, *Int. J. Rock Mech. Min. Sci. Geomech. Abstr.*, *30*, 789–795.

Dieterich, J. H. (1992), Earthquake nucleation on faults with rate and state-dependent friction, *Tectonophysics*, *211*, 115–34.

Garcia, J., M. Walters, J. Beall, C. Hartline, A. Pingol, S. Pistone, and M. Wright (2012), Overview of the Northwest Geysers EGS demonstration project Proceedings, 37th Workshop on Geothermal Reservoir Engineering, Stanford Univ., Stanford, Calif., 30 Jan.–1 Feb.

Guglielmi, Y., F. Cappa, and D. Amitrano (2008), High definition analysis of fluid-induced seismicity related to the mesoscale hydromechanical properties of a fault zone, *Geophys. Res. Lett.*, *35*, L06306, doi:10.1029/2007GL033087.

Hsiung, S. M., A. H. Chowdhury, and M. S. Nataraja (2005), Numerical simulation of thermal-mechanical processes observed at the Drift-Scale Heater Test at Yucca Mountain, Nevada, USA, *Int. J. Rock Mech. Min. Sci.*, *42*(5–6), 652–666.

Hulen, J. B., and D. L. Norton (2000), Wrench-fault tectonics and emplacement of the Geysers felsites, *Geotherm. Resour. Counc. Trans.*, *24*, 289–298.

International Formulation Committee (1967), *A Formulation of the Thermodynamic Properties of Ordinary Water Substance*, IFC Secretariat, Dusseldorf, Germany.

Itasca (2009), FLAC3D, fast Lagrangian analysis of continua in 3 dimensions version 4.0. Minneapolis, Minnesota, Itasca Consulting Group.

Jaeger, J. C., and N. G. W. Cook (1979), *Fundamentals of Rock Mechanics*, 3rd ed., 590 pp., CRC Press, Boca Raton, Fla.

Jeanne, P., J. Rutqvist, C. Hartline, J. Garcia, P. F. Dobson, and M. Walters (2014a), Reservoir structure and properties from geomechanical modeling and microseismicity analyses associated with an Enhanced Geothermal System at The Geysers, California, *Geothermics*, *51*, 460–469.

Jeanne, P., J. Rutqvist, D. Vasco, J. Garcia, P. F. Dobson, M. Walters, C. Hartline, and A. Borgia (2014b), A 3D hydrogeological and geomechanical model of an enhanced geothermal system at The Geysers, California, *Geothermics*, *51*, 240–252.

Jeanne, P., J. Rutqvist, P. F. Dobson, J. Garcia, M. Walters, and C. Hartline (2014c), The impacts of mechanical stress transfers caused by hydromechanical and thermal processes on fault stability during hydraulic stimulation in a deep geothermal reservoir, *Int. J. Rock Mech. Min. Sci.*, *72*, 149–163.

Johnson, L. (2014), A source model for induced earthquakes at the Geysers geothermal reservoir, *Pure Appl. Geophys.*, *171*(8), 1625–1640, doi:10.1007/s00024-014-0798-7.

Koh, J., H. Rosnhan, and S. S. Rahman (2011), A numerical study on the long term thermo-poroelastic effects of cold water injection into naturally fractured geothermal reservoirs, *Comput. Geotech.*, *38*, 669–82.

Liu, H. H., J. Rutqvist, G. Zhou, and G. S. Bodvarsson (2004), Upscaling of normal stress-permeability relationship for fracture network obeying the fractional levy motion, in *Coupled THMC Processes in Geo-system: Fundamentals, Modelling, Experiments and Applications*, edited by O. Stephansson, J. A. Hudson, and L. Jing, pp. 263–268, Elsevier, Oxford, U. K.

Lockner, D. A., R. Summer, D. Moore, and J. D. Byerlee (1982), Laboratory measurements of reservoir rock from the Geysers Geothermal Field, California, *Int. J. Rock Mech. Min. Sci.*, *19*, 65–80.

Majer, E. L., and J. E. Peterson (2007), The impact of injection on seismicity at The Geysers, California Geothermal Field, *Int. J. Rock Mech. Min. Sci.*, *44*, 1079–1090.

Makurat, A., N. Barton, L. Tunbridge, and G. Vik (1990), The measurements of the mechanical and hydraulic properties of rock joints at different scale in the Stripa project, in *Proceedings of the International Symposium on Rock Joints, Loen, Norway, 4–7 June 1990*, edited by N. Barton and O. Stephansson, pp. 541–8, Balkema, Rotterdam.

Min, K. B., J. Rutqvist, C.-F. Tsang, and L. Jing (2004), Stress-dependent permeability of fracture rock masses: A numerical study, *Int. J. Rock Mech. Min. Sci.*, *41*, 1191–210.

Mossop, A., and P. Segall (1997), Subsidence at The Geysers Geothermal Field, N. California from a comparison of GPS and leveling surveys, *Geophys. Res. Lett.*, *24*, 1839–1842, doi:10.1029/97GL51792.

Nielson, D. L., M. A. Walters, and J. B. Hulen (1991), Fracturing in the Northwest Geysers, Sonoma County, California, *Geotherm. Resour. Counc. Trans.*, *15*, 27–33.

Olsson, R., and N. Barton (2001), An improved model for hydromechanical coupling during shearing of rock joints, *Int. J. Rock Mech. Min. Sci.*, *38*(3), 317–329.

Oppenheimer, D. C. (1986), Extensional tectonics at The Geysers Geothermal Area, California, *J. Geophys. Res.*, *91*, 11,463–11,476, doi:10.1029/JB091iB11p11463.

Parotidis, M., S. A. Shapiro, and E. Rothert (2004), Back front of seismicity induced after termination of borehole fluid injection, *Geophys. Res. Lett.*, *31*, L02612, doi:10.1029/2003GL018987.

Pruess, K., C. Oldenburg, and G. Moridis (2011), TOUGH2 User's Guide, Version 2.1, LBNL-43134 (revised) Lawrence Berkeley National Laboratory, Berkeley, Calif.

Rinaldi, A. P., J. Rutqvist, E. Sonnenthal, and T. Cladouhos (2014), Coupled THM modeling of hydroshearing stimulation in tight fractured volcanic rock, *Transp. Porous Media*, *108*, 131–150.

Rutqvist, J. (2011), Status of the TOUGH-FLAC simulator and recent applications related to coupled fluid flow and crustal deformations, *Comput. Geosci.*, *37*, 739–750.

Rutqvist, J. (2015), Fractured rock stress-permeability relationships from in situ data and effects of temperature and chemical-mechanical couplings, *Geofluids*, *15*, 48–66, doi:10.1111/gfl.12089.

Rutqvist, J., and O. Stephansson (2003), The role of hydromechanical coupling in fractured rock engineering, *Hydrogeol. J.*, *11*, 7–40.

Rutqvist, J., Y.-S. Wu, C.-F. Tsang, and G. Bodvarsson (2002), A modeling approach for analysis of coupled multiphase fluid flow, heat transfer, and deformation in fractured porous rock, *Int. J. Rock Mech. Min. Sci.*, *39*, 429–442.

Rutqvist, J., C. Leung, A. Hoch, Y. Wang, and Z. Wang (2013), Linked multicontinuum and crack tensor approach for modeling of coupled geomechanics, fluid flow and transport in fractured rock, *J. Rock Mech. Geotech. Eng.*, *5*, 18–31.

Rutqvist, J., P. F. Dobson, J. Garcia, C. Hartline, P. Jeanne, C. M. Oldenburg, D. W. Vasco, and M. Walters (2015), The Northwest Geysers EGS demonstration project, California: Pre-stimulation modeling and interpretation of the stimulation, *Math. Geosci.*, *15*, 48–66, doi:10.1007/s11004-013-9493-y.

Schoenball, M., T. M. Müller, B. I. R. Müller, and O. Heidbach (2010), Fluid-induced microseismicity in pre-stressed rock masses, *Geophys. J. Int.*, *180*(2), 813–819, doi:10.1111/j.1365-246X.2009.04443.x.

Shapiro, S., E. Rothert, V. Rath, and J. Rindschwentner (2002), Characterization of fluid transport properties of reservoirs using induced microseismicity, *Geophysics*, *67*, 212–220, doi:10.1190/1.1451597.

Shapiro, S. A., and C. Dinske (2009), Fluid-induced seismicity: Pressure diffusion and hydraulic fracturing, *Geophys. Prospect.*, *57*(2), 301–310, doi:10.1111/j.1365-2478.2008.00770.x.

Shapiro, S. A., E. Huenges, and G. Borm (1997), Estimating the crust permeability from fluid-injection-induced seismic emission at the KTB site, *Geophys. J. Int.*, *131*(2), F15–F18, doi:10.1111/gji.1997.131.

Sibson, R. H., and J. V. Rowland (2003), Stress, fluid pressure and structural permeability in seismogenic crust, North Island, New Zealand, *Geophys. J. Int.*, *154*, 584–594, doi:10.1046/j.1365-246X.2003.01965.x.

Stark, M. A. (2003), Seismic evidence for a long-lived enhanced geothermal system (EGS) in the Northern Geysers Reservoir, *Geotherm. Resour. Counc. Trans.*, *27*, 727–731.

Terzaghi, K. (1923), Die Berechnung der Durchlässigkeitsziffer des Tones aus dem Verlauf der hydrodynamischen Spannungserscheinungen, *Sitzungsbericthe Kais. Akad. Wiss. Wien*, *132*, 105.

Verdon, P. P., J. M. Kendall, D. J. White, and D. A. Angus (2011), Linking microseismic event observations with geomechanical models to minimize the risks of storing CO_2 in geological formations, *Earth Planet. Sci. Lett.*, *305*, 143–152.

Zhao, Z., J. Rutqvist, C. Leung, M. Hokr, I. Neretnieks, A. Hoch, J. Havlcek, Y. Wang, Z. Wang, and R. Zimmerman (2013), Stress effects on solute transport in fractured rocks: A comparison study, *J. Rock Mech. Geotech. Eng.*, *5*, 110–23.